Energy Storing Electrical Cables: Integrating Energy Storage and Electrical Conduction

*Zenan Yu and Jayan Thomas**

Currently, millions of miles of electrical cables have been used for providing electrical connections in machineries, equipment, buildings and other establishments. Energy storage devices are completely separated from these electrical cables if used. However, it will revolutionize energy storage applications if both electrical conduction and energy storage can be integrated into the same cable. Coaxial cable, also called coax, is one of the most common and basic cable designs that is used to carry electricity or signal. It has an inner conductor enclosed by a layer of electrical insulator, and covered by an outer tubular conducting shield (see Supporting Information, SI, Figure S1). The term "coaxial" is used because both the inner and outer conductors share the same geometric axis. In a coaxial design, it is possible to combine two different functional devices into one device that can still perform the original functions independently.

Supercapacitors, also known as electrochemical capacitors, have become one of the most popular energy storage devices in recent years. Compared to other energy storage devices like batteries, supercapacitors have faster charge-discharge rates, higher power densities, and longer life times.[1] As a signature of their performance, safety, and reliability, they have recently been employed in the emergency doors of Airbus A380. Supercapacitors store energy by Faradaic or non-Faradaic reactions. Supercapacitors which utilize the Faradaic reactions are also called pseudocapacitors. Metal oxides/hydroxides like ruthenium oxide (RuO_2),[2] manganese dioxide (MnO_2),[3] cobalt oxide (Co_3O_4),[4] nickel oxide (NiO),[5] and nickel hydroxide ($Ni(OH)_2$),[6] have been extensively studied as electrode materials in pseudocapacitors. Among them, MnO_2 has stood out due to its outstanding characteristics such as high theoretical specific capacitance (~1,400 F g^{-1}), natural abundance, and environmental friendliness.[7] However, the poor electrical conductivity of MnO_2 (~10^{-5} – 10^{-6} S cm^{-1}) is a limiting factor in achieving its theoretical specific capacitance.[7b,8] One feasible approach proposed by Simon and Gogotsi is depositing pseudocapacitive material (like MnO_2) onto a nanostructured current collector.[9] Despite some achievements that have been made by using similar methods, such as depositing MnO_2 onto nanowires,[10] nanotubes,[11] and nanopillars,[12] these arrays usually suffer from structural collapse, resulting in a decrease of useful surface area, reduction of deposited active materials and limited accessibility of electrolyte. Furthermore, these nanostructured current collectors are either derived from expensive and environment-unfriendly template methods or tedious fabrication processes. Therefore, it is still a challenge to readily and simply fabricate nanostructured electrodes with large area, template-free, and high aspect ratio arrays without nanostructures clumping together.

Here we developed a large area, template-free, high aspect ratio, and freestanding CuO@AuPd@MnO_2 core-shell nanowhiskers (NWs) design. Our electrochemical measurements show that these CuO@AuPd@MnO_2 NWs exhibit remarkable properties including high specific capacitance, excellent reversible redox reactions, and fast charge-discharge ability. Moreover, a novel coaxial supercapacitor cable (CSC) design which combines electrical conduction and energy storage by modifying the copper core used for electrical conduction was demonstrated. For accomplishing large surface area necessary for high supercapacitor performance, we developed NWs on the outer surface of the electrical copper wire. The NWs structure is developed by just heating the inner core and therefore is practical to upscale the process to make extended lengths. An attractive advantage of using the coaxial design is that electricity can be conducted through the inner conductive metal wire and electrical energy can be stored in the nanostructured concentric layers added to this inner metal wire with an oxide layer in between. It is always a vital task for many applications including aviation to find better methods to save weight and space, while maintaining the intended purpose. Therefore, integration of electrical cable and energy storage device into one unit offers a very promising opportunity to transmit electricity and store energy at the same time. In addition, CSC built from these NWs exhibits excellent flexibility and bendability, superior long-term cycle stability, and high power and energy densities. The development of this innovative lightweight, flexible, and space saving CSC will be very attractive for many applications including hybrid and all-electric vehicles, electric trains, heavy machineries, aircrafts and military.

Fabrication of electrode involves three steps: (1) growth of CuO NWs from a pure copper wire by heat treatment; (2) deposition of a conducting metal layer by sputter-coating; (3) electrodeposition of active material onto the nanostructures (**Figure 1**a). Scanning electron microscope (SEM) image (Figure 1b) clearly

Z. Yu, Prof. J. Thomas
NanoScience Technology Center
University of Central Florida
Florida 32826, USA
E-mail: Jayan.Thomas@ucf.edu
Z. Yu, Prof. J. Thomas
Department of Materials Science and Engineering
University of Central Florida
Florida 32826, USA
Prof. J. Thomas
CREOL, College of Optics and Photonics
University of Central Florida
Florida 32826, USA

DOI: 10.1002/adma.201400440

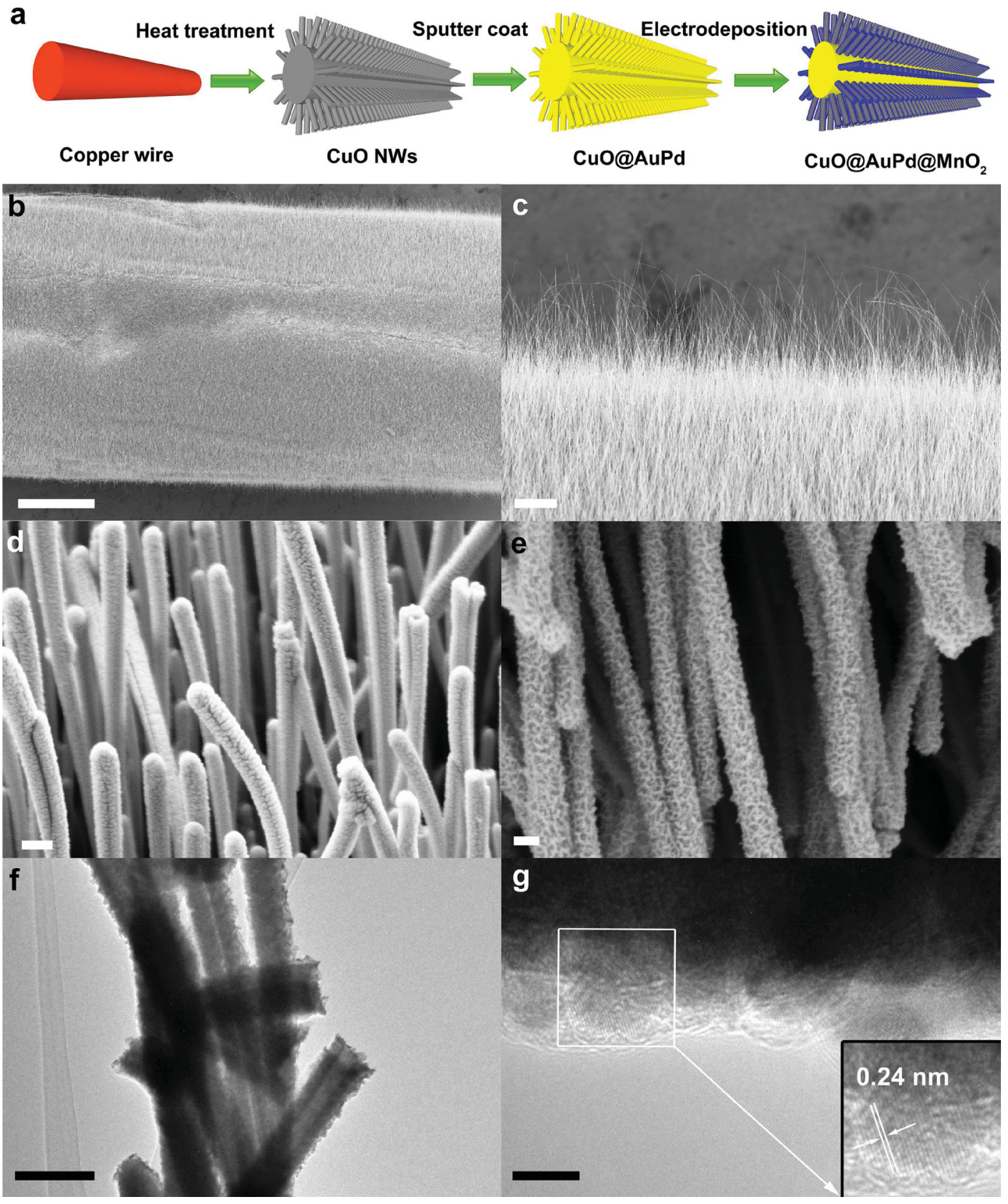

Figure 1. (a) Schematic illustration showing the fabrication process of CuO@AuPd@MnO_2 NWs. (b) Top view of SEM image shows that the copper wire is completely covered by CuO NWs. Scale bar, 100 μm. (c) Close-up view of SEM image showing vertically grown CuO NWs. Scale bar, 10 μm. (d) SEM image of AuPd nanoparticles that were conformally sputter-coated onto each NW. Scale bar, 300 nm. (e) SEM image of MnO_2 that was uniformly electrodeposited onto NWs. Scale bar, 200 nm. (f) Low-magnification TEM image of CuO@AuPd@MnO_2 NWs. Scale bar, 200 nm. (g) HRTEM image of CuO@AuPd@MnO_2 NW. Scale bar, 5 nm. The inset is the enlarged HRTEM image of the rectangular area.

shows that CuO NWs were grown uniformly on the Cu wire (diameter of ~0.37 mm) when heated at 500 °C for 4 hours. The average lengths of CuO NWs are ~15 μm and diameter is ~ 100 nm (Figure 1c). Prior to depositing active material, a thin layer of gold-palladium (AuPd; 60% Au: 40% Pd) was deposited onto the CuO NWs to serve as a current collector as well as an anode for electro-deposition of active material. Metal deposition is necessary since CuO is a poor conductor of electricity. This insulating effect of CuO is beneficial in limiting the current leakage from the inner core. It can be noted that the surface of CuO NW became grainier after deposition of AuPd (Figure 1d) which enhances the surface area to a small extent. It is also worth noting that any other metal, such as copper, can be used to provide the same function as AuPd (SI, Figure S2). MnO_2 was then conformally electrodeposited onto these NWs (Figure 1e). The detailed structure of CuO@AuPd@MnO_2 NWs was further examined by high-resolution transmission electron microscopy (HRTEM). Figure 1f shows a low-magnification TEM image of CuO@AuPd@MnO_2 NWs which agrees well with the SEM in Figure 1e. A HRTEM image was shown in Figure 1g, from which a thin MnO_2 film uniformly covering the surface of CuO NWs can be clearly identified. The inset of Figure 1g indicates the crystallinity of metal nanoparticles that were sputtered (with a fringe spacing of ~0.24 nm); while no clear fringe spacing was observed for the MnO_2 outer film, revealing the amorphous characteristic of MnO_2. Moreover, energy-dispersive X-ray spectroscopy (EDS) mapping (SI, Figure S3) further confirms the core-shell structure of CuO@AuPd@MnO_2 NWs. The chemical composition of as-electrodeposited MnO_2 was analyzed using X-ray photoelectron spectroscope (XPS) and only two peaks corresponding to Mn^{4+} oxidation state were found (SI, Figure S4), indicating Mn^{4+} ions are the main components of the electrodeposited layer. A similar fabrication technique is used to make NW on a flexible copper foil (SI, Figure S5). SEM images of a tubular outer electrode derived from copper foil are shown in SI, Figure S6. The thickness of the outer electrode is ~30 μm and vertically grown NWs can be clearly found on the inner side of the outer electrode.

To evaluate the electrochemical properties of CuO@AuPd@MnO_2 NWs, cyclic voltammetry (CV) measurements were performed using a three-electrode system in 1M KOH solution. For comparison, pure CuO NWs and CuO@AuPd NWs were also studied using CV measurements (SI, Figure S7). CV curve of CuO@AuPd@MnO_2 NWs has much higher current compared to pure CuO and CuO@AuPd NWs, revealing CuO@AuPd@MnO_2 has the best supercapacitive behavior (**Figure 2**a). CV curves of CuO@AuPd@MnO_2 NWs at different scan rates ranging from 5 to 100 mV s^{-1} were also performed and shown in Figure 2b. All the CV curves are close to a symmetrical rectangle-like shape, indicating good electrochemical performance of CuO@AuPd@MnO_2 NWs. Different mass loading of MnO_2 were also studied by varying the deposition time ranging from 3 to 48 min. All the CV curves of different deposition time show good rectangularity (Figure 2c), implying the good capacitive behavior of the electrodes. The specific capacitance for 3, 6, 12, 24, 48 min deposition of MnO_2 was 1,376, 702, 562, 561, and 493 F g^{-1} (based on MnO_2), respectively, at a scan rate of 5 mV s^{-1} (Figure 2d). Calculation of

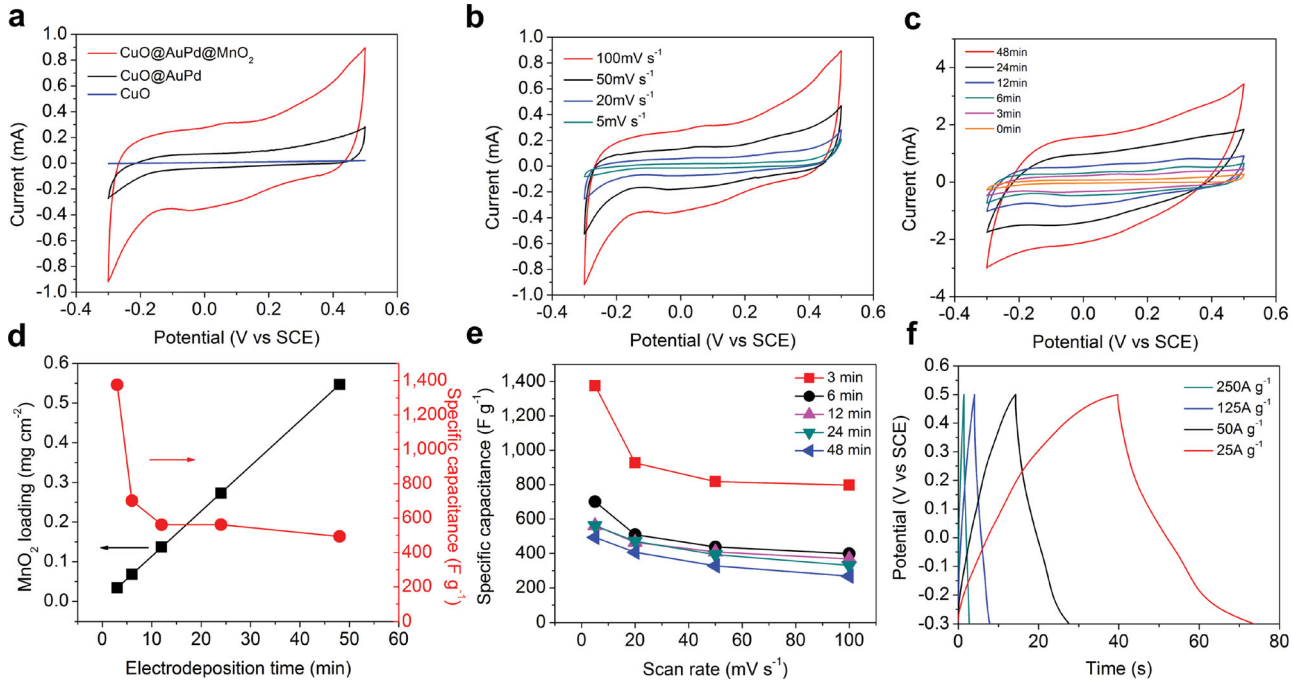

Figure 2. (a) CV curves of CuO@AuPd@MnO_2 NWs compared to pure CuO NWs and CuO@AuPd NWs at a scan rate of 100 mV s^{-1} in 1M aqueous KOH electrolyte. (b) CV curves of CuO@AuPd@MnO_2 NWs at different scan rates (5 – 100 mV s^{-1}). (c) CV curves of CuO@AuPd@MnO_2 NWs at a scan rate of 100 mV s^{-1} with different MnO_2 deposition time of 0, 3, 6, 12, 24, and 48 min, respectively. (d) MnO_2 loading and specific capacitance at a scant rate of 5 mV s^{-1} of CuO@AuPd@MnO_2 NWs as a function of electrodeposition time. (e) Specific capacitance of CuO@AuPd@MnO_2 NWs at different MnO_2 electrodeposition times as a function of scan rate. (f) GCD curves of CuO@AuPd@MnO_2 NWs at different current densities (25 – 250 A g^{-1}).

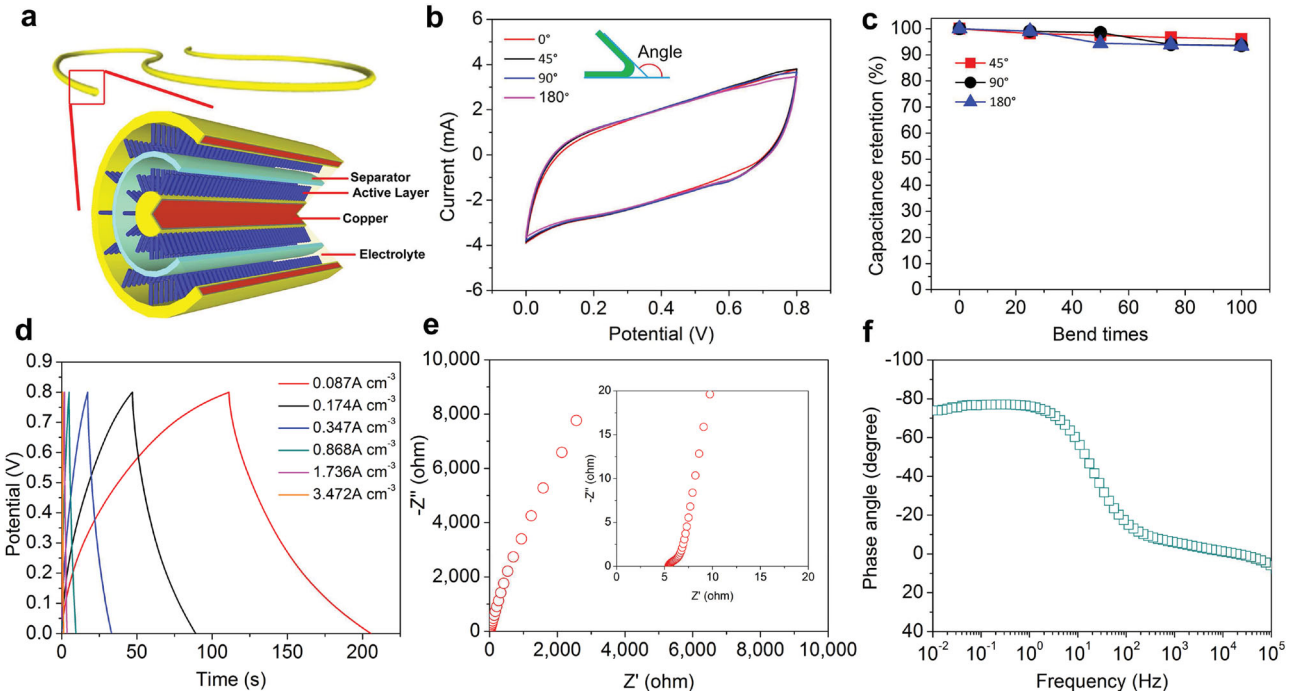

Figure 3. (a) A schematic diagram of CSC using solid electrolyte. (b) Subtle changes of CV curves collected at a scan rate of 100 mV s^{-1}, under different bending angles ranging from 0 – 180°. (c) Bending the device up to 100 times at different bending angles showing excellent bendability of our devices. (d) GCD curves of device at different current densities. (e) Nyquist plots of the CSC. (f) Bode plots of the CSC.

specific capacitance is based on subtraction of the capacitance which belongs to the AuPd from the total capacitance (Detailed calculation can be found in the SI). The highest specific capacitance of 1,376 F g^{-1} was obtained for a 3 min deposition of MnO_2 (mass loading of 0.04 mg cm^{-2}). This value is much higher than other MnO_2 based nanostructures, such as SnO_2@MnO_2 nanowires (637 F g^{-1} at 2 mV s^{-1}, 0.08 mg cm^{-2}),[13] AuPd@MnO_2 nanopillars (603 F g^{-1} at 5 mV s^{-1}, 0.01 mg cm^{-2}),[12a] WO_{3-x}@Au@MnO_2 nanowires (588 F g^{-1} at 10 mV s^{-1}, 0.04 mg cm^{-2}),[14] TiN/MnO_2 nanotubes (486 F g^{-1} at 2 mV s^{-1}, 0.06 mg cm^{-2}),[15] C@MnO_2 nanorods (302 F g^{-1} at 5 mV s^{-1}, 0.072 mg cm^{-2}),[16] and Zn_2SnO_4@MnO_2 nanorods (621.6 F g^{-1} at 2 mV s^{-1}).[17] In addition, the specific capacitance of our electrode still remained at 493 F g^{-1} even at a higher loading mass of MnO_2 (0.55 mg cm^{-2}). The specific capacitance of electrodes with a deposition time of 3 min show consistent enhancement of up to 2 times than those with longer deposition times by varying the scan rate from 5 to 100 mV s^{-1} (Figure 2e). This implies that the elongating deposition times may lead to an increase in thickness of active material (SI, Figure S8), but the condensed packing will result in surface area overlap of MnO_2. In this case, the whole surface area of MnO_2 cannot be fully charged or discharged.

To further evaluate the charge-discharge storage capacity of our electrodes, galvanostatic charge-discharge (GCD) measurements were performed using the same three-electrode configuration system as the CV measurements. GCD curves of the CuO@AuPd@MnO_2 NWs at different current densities (25 – 250 A g^{-1}) show linear and symmetrical charge and discharge profiles (Figure 2f), indicating good supercapacitve behavior of these NWs. Different deposition times of MnO_2 were also studied by GCD (SI, Figure S9). The specific capacitance achieved by depositing MnO_2 for 3, 6, 12, 24, 48 min at a current density of 1 mA cm^{-2} is 857, 564, 556, 542, 498 F g^{-1}, respectively. The specific capacitance obtained for a 3 min deposition time is much higher than those obtained for a longer deposition time which is in accordance with the result from CV measurements. The electrochemical properties of CuO@AuPd@MnO_2 NWs were further analyzed by electrochemical impedance spectroscopy (EIS) as shown in Figure S10. The straight line of Nyquist plots and small resistance of electrode indicates excellent electrochemical behavior of CuO@AuPd@MnO_2 NWs.

A solid state CSC is simply fabricated by placing the outer tubular electrode onto the inner electrode (both pre-coated with gel electrolyte) where the two electrodes are separated by an ion porous separator (**Figure 3**a). CV measurements were also performed to test the flexibility and bendability of CSC. Figure 3b shows the CV curves of our device tested under different bending angles ranging from 0 to 180 degrees. The shapes of all four CV curves are almost identical to one another, indicating the good flexibility of our device. Moreover, the rectangular and symmetrical shape of the CV curves exhibits ideal pseudocapacitive nature of MnO_2 and superior reversible redox reaction. A bend test of our devices was also carried out by folding the device at different angles up to 100 times. The supercapacitor device remained at 93.4% of its initial capacitance even after folding at 180 degree for 100 times (Figure 3c), revealing the excellent bendability of our device. To further evaluate the electrochemical performance of our device, GCD measurements were performed. Figure 3d exhibits the GCD curves at various current densities ranging from 0.087 to 3.472 A cm^{-3}. The charge-discharge curves are symmetric and

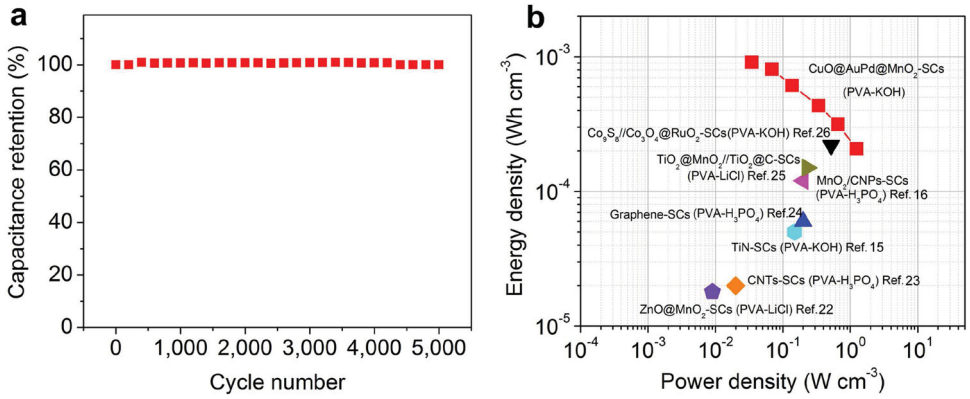

Figure 4. (a) Cycle performance of the device at a scan rate of 100 mV s^{-1} for 5,000 cycles. (b) Power and energy densities of the device.

linear in nature further confirms the good electrochemical capacitive characteristics and fast charging-discharging process which is a characteristic of CSC. The electrochemical performance of CSC is further evaluated using EIS with frequency ranging from 10 mHz to 100 kHz. The Nyquist plots (Figure 3e) shows a straight line which indicates an ideal capacitive behavior of CSC. Moreover, the resistance of the device is very close to the intercept of the Nyquist curve on the real axis (the inset of Figure 3e), demonstrating the low internal resistivity of the electrode and good conductivity of the electrolyte. Figure 3f displays the Bode plots of the CSC. The phase angle is close to –90° for frequency up to 5 Hz, suggesting an ideal capacitor is approached for CSC. The relaxation time (59 ms) is calculated based on the frequency (17 Hz) that possesses a phase angle of –45° at which point that the capacitive and resistive impedances are equal.[18] The fast frequency response may attribute to the large and accessible surface area of the CSC. This exceptional tiny time constant for the CSC shows very competitive potential compared with other reported values for supercapacitors such as activated carbon (700 ms),[19] MnO_2/carbon composite (500 ms),[16] PEDOT/CNT (80 ms),[20] graphene (19 ms),[21] onion-like carbon (26 ms),[19] etc.

Good cycling performance is one of the vital characteristics for energy storage devices. **Figure 4**a shows the long-term cycle stability of CSC at a scan rate of 100 mV s^{-1}. The capacitance still remains at 99% of its initial value after 5000 cycles, revealing its excellent cycle stability. Energy density and power density are the other two important parameters to characterize the performance of energy storage devices. Figure 4b presents the volumetric power and energy densities of the solid electrolyte based CSC. The average volumetric energy density is 0.55 mWh cm^{-3} with a volumetric power density of 413 mW cm^{-3}. These results are substantially higher than that of the recently reported all-solid-state supercapacitors (SCs), such as ZnO@MnO_2-SCs (0.018 mWh cm^{-3} and 9 mW cm^{-3}, PVA-LiCl),[22] carbon nanotube SCs (CNT-SCs, 0.02 mWh cm^{-3} and 20 mW cm^{-3}, PVA-H_3PO_4),[23] TiN SCs (0.05 mWh cm^{-3} and 150 mW cm^{-3}, PVA-KOH),[15] Graphene-SCs (0.06 mWh cm^{-3} and 200 mW cm^{-3}, PVA-H_3PO_4),[24] MnO_2/carbon-nanoparticles SCs (MnO_2/CNPs-SCs, 0.12 mWh cm^{-3} and 200 mW cm^{-3}, PVA-H_3PO_4),[16] TiO_2@MnO_2 and TiO_2@C asymmetric SCs (TiO_2@MnO_2//TiO_2@C-SCs, 0.15 mWh cm^{-3} and 230 mW cm^{-3}, PVA-LiCl),[25] and Co_9S_8//Co3O4@RuO_2-SCs (0.22 mWh cm^{-3} and 520 mW cm^{-3}, PVA-KOH).[26]

Superior electrochemical performance of CSC can be attributed to three factors. First, surface area of each electrode is significantly enhanced by nanoarchitecturing, which provides much more electrochemical-active sites for the reversible redox reactions. As shown in Figure 1b and c, CuO NWs were vertically grown on the copper wire, which increases the surface area immensely compared to a smooth surface of copper wire (more than 2 orders of magnitude enhancement, see Supporting Information). After depositing active material onto this nanostructure, more electrochemically active sites will be used during charge-discharge process compared to a non-nanostructured surface. This results in substantial improvements of electrochemical properties. Second, NW structure provides more open space, which facilitates the accessibility of electrolyte. As shown in Figure 1e, MnO_2 was conformally coated onto NWs and each NW is completely separated without touching each other, which enables the electrolyte to access the MnO_2 from the bottom site of each NW. Third, the internal resistance is sharply reduced by the large and binder-free contact area between AuPd and MnO_2. When depositing MnO_2 onto a non-nanostructured surface, the condensed packing of MnO_2 will block electrons from reaching the first layer of MnO_2, whereas the path for electron transport will be significantly shortened through the use of a nanostructured design.

Experiments were designed to demonstrate the dual functionality of CSC, i.e. it functions as both electrical cable and energy storage device. Also, it was our intention to demonstrate that the two functions do not affect each other when operated simultaneously. We measured the voltage of pre-charged energy storage section of CSC, and, at the same time, connected the inner electrical cable to an outside electrical circuit which involves a power and a LED (SI, Figure S11a). Before we turned on the power (LED off), the voltage of the energy storage section was 0.786 V, indicating charge holding state of energy storage section (SI, Figure S11b). After we turned on the power (LED on), the voltage still remained at 0.791 V (SI, Figure S11c), indicating that the electrical cable section does not interfere the charge holding capability of energy storage section. Moreover, we also connected the energy storage section to an electrochemical work station, before and after turning on the power (SI, Figure S11d and S11e). CV curves kept almost the same for the two different states, which further demonstrates the independence of the energy storage section from the inner electrical cable (SI, Figure S11f).

In order to demonstrate that the energy storage section does not influence the function of the inner electrical cable section, we measured the electrical resistance using two-probe method. The current-voltage (I-V) curves of the inner electrical cable exhibit the same slope before and after the energy storage section is charged, manifesting the independence of the inner electrical cable (SI, Figure S12a). These experiments demonstrate the dual functionality of CSC. Additionally, our inner electrical cable has the same slope compared to a pure copper wire (both with lengths of 1cm), revealing a good conductivity of the inner electrical cable. However, I-V curve of the outer CuO layer as shown in Figure S12b exhibits large resistance (~2.23 MΩ, length 1 cm).

The key to the high performance of this integrated design is the CuO NWs layer. It involves two attractive advantages: (1) AuPd conducting layer (serves as current collector in supercapacitor) and the copper core conductor is insulated by the CuO layer (thickness ~2 μm, SI, Figure S13). This layer prevents the core cable and supercapacitor to interfere with each other. In other words, if active material is directly deposited onto the conductors without this CuO layer, the function of core cable cannot be performed because electrons transmitting through will be leaked and consumed by electrochemical reactions. (2) CuO NWs serves as nanostructured scaffold for depositing AuPd and MnO_2 respectively, which provides an efficient strategy for overcoming the low conductivity of MnO_2.

In summary, we have developed a novel integrated CSC that serves as an energy storage device as well as an electrical conduction cable. CuO@AuPd@MnO_2 core-shell NWs as electrode of the energy storage part of CSC exhibits excellent electrochemical properties, in which case a specific capacitance of 1376 F g^{-1} was obtained at a scan rate of 5 mV s^{-1}. Moreover, CSC base on CuO@AuPd@MnO_2 NWs show extraordinary flexibility and bendability, more than 99% capacitance retention (even after 5000 cycles), and high power and energy densities (0.55 mWh cm^{-3} and 413 mW cm^{-3}). Aside from its excellent electrochemical performance, coaxial design of the supercapacitor enables it to be integrated with the electrical cable to make long lengths. All these results demonstrate that CSC can have high impact on the future energy storage applications.

Experimental Section

Fabrication of Electrodes: CuO NWs can be easily grown on copper wire/foil by a simple heat treatment in air.[27] A pure copper wire/foil was cleaned in an acetone solution for 1 min, followed by washing with distilled (DI) water twice and drying by a nitrogen gas flow. The copper wire/foil was then placed in an alumina crucible and rapidly heated to 500 °C at a heating rate of 20 °C min^{-1} in a MTI Muffle furnace and kept for 4 h. After heat treatment, the sample was placed in a sputter coater (EMITECH K550) for metal deposition at a constant current of 40 mA for 20 min. The target used for sputtering is composed of 60% Au and 40% Pd. MnO_2 active layer was deposited onto the conducting AuPd metal layer using an anodic electrodeposition method at constant current of 0.5 mA cm^{-2} for 3 – 48 min. The electrolyte for electrodeposition was prepared by mixing 0.01 M manganese acetate ($MnAc_2$) and 0.02 M ammonium acetate (NH_4Ac) in a solvent containing 90 v/v% of DI water and 10 v/v% of dimethyl sulfoxide (DMSO).

Fabrication of CSC: The gel electrolyte was prepared by dissolving 5.6 g KOH and 10 g PVA in 100 mL DI water. The whole mixture was heated at 90 °C under stirring until all the solute completely dissolves in the solvent. The viscous electrolyte solution was carefully coated onto the MnO_2 deposited area of both inner and outer electrodes with a working length of 1 cm. The outer electrode was then tightly surrounded onto the inner electrode with an ion porous separator (Celgard 3501, NC, 25 μm) in between. After the PVA-KOH gel electrolyte solidified at room temperature, a solid-state CSC was prepared.

Characterization and Measurements: Surface morphologies were characterized by means of scanning electron microscopy (SEM, ZEISS Ultra 55) and transmission electron microscopy (TEM, TECNAI F30) equipped with an energy-dispersive X-ray spectroscopy (EDS). To investigate the chemical compositions of sample surface, X-ray photoelectron spectroscopy (XPS, PHI 5400) was performed. To compare the electrochemical performance of different materials, a three-electrode system consisting of a working electrode (based on the materials prepared), a platinum counter electrode and a saturated calomel electrode (SCE) as reference electrode was used. Cyclic voltammetry (CV) and galvanostatic charge-discharge (GCD) measurements were performed using this three-electrode configuration in 1M KOH solution on an electrochemical workstation (Bio-Logic, SP-150). The characterization experiments of the devices using solid electrolyte were conducted by a two-electrode system in air at a voltage range of 0–0.8 V. Electrochemical impedance spectroscopy (EIS) measurements were performed by applying an AC voltage with 5 mV amplitude in a frequency range from 10 mHz to 100 kHz. All the calculations including specific capacitance as well as energy and power densities are discussed in detail in the supplementary information.

Supporting Information

Schematics, EDS, XPS, SEM, TEM, dual functionality demonstration, EIS, CV and GCD curves, experimental details, and capacitive equations. Supporting Information is available from Wiley Online Library or from the author.

Acknowledgements

J.T acknowledges Florida Space Institute for the SRI funding for the partial fulfillment of this work. The authors thank Materials Characterization Facility (MCF), University of Central Florida for the nanostructure characterization.

Received: January 27, 2014
Revised: February 28, 2014
Published online: March 27, 2014

[1] a) M. Winter, R. J. Brodd, *Chem. Rev.* **2004**, *104*, 4245; b) J. R. Miller, P. Simon, *Science* **2008**, *321*, 651; c) J. R. Miller, A. F. Burke, *Electrochem. Soc. Interface* **2008**, *17*, 53; d) M. D. Stoller, S. Park, Y. Zhu, J. An, R. S. Ruoff, *Nano Lett.* **2008**, *8*, 3498; e) L.-Q. Mai, F. Yang, Y.-L. Zhao, X. Xu, L. Xu, Y.-Z. Luo, *Nat. Commun.* **2011**, *2*, 381; f) B. Duong, Z. Yu, P. Gangopadhyay, S. Seraphin, N. Peyghambarian, J. Thomas, *Adv. Mater. Interfaces* **20142014**, *1*, 1300014.
[2] Y.-S. Hu, Y.-G. Guo, W. Sigle, S. Hore, P. Balaya, J. Maier, *Nat. Mater.* **2006**, *5*, 713.
[3] a) X. Lang, A. Hirata, T. Fujita, M. Chen, *Nat. Nanotechnol.* **2011**, *6*, 232; b) R. Liu, F. Wong, W. Duan, A. Sen, *Adv. Mater.* **2013**, *25*, 6997; c) A. Sumboja, C. Y. Foo, X. Wang, P. S. Lee, *Adv. Mater.* **2013**, *25*, 2809.
[4] T. Zhu, J. S. Chen, X. W. Lou, *J. Mater. Chem.* **2010**, *20*, 7015.
[5] G. Wang, L. Zhang, J. Zhang, *Chem. Soc. Rev.* **2012**, *41*, 797.

[6] a) H. Li, M. Yu, F. Wang, P. Liu, Y. Liang, J. Xiao, C. Wang, Y. Tong, G. Yang, *Nat. Commun.* **2013**, *4*, 1894; b) H. Wang, Y. Liang, T. Mirfakhrai, Z. Chen, H. S. Casalongue, H. Dai, *Nano Research* **2011**, *4*, 729.

[7] a) M. Toupin, T. Brousse, D. Bélanger, *Chem. Mater.* **2004**, *16*, 3184; b) D. Bélanger, L. Brousse, J. W. Long, *Electrochem. Soc. Interface* **2008**, *17*, 49; c) G. Yu, L. Hu, M. Vosgueritchian, H. Wang, X. Xie, J. R. McDonough, X. Cui, Y. Cui, Z. Bao, *Nano Lett.* **2011**, *11*, 2905; d) T. Brousse, M. Toupin, R. Dugas, L. Athouël, O. Crosnier, D. Bélanger, *J. Electrochem. Soc.* **2006**, *153*, A2171; e) V. Subramanian, H. Zhu, R. Vajtai, P. M. Ajayan, B. Wei, *J. Phys. Chem. B* **2005**, *109*, 20207.

[8] a) W. Wei, X. Cui, W. Chen, D. G. Ivey, *Chem. Soc. Rev.* **2011**, *40*, 1697; b) Y. Cheng, S. Lu, H. Zhang, C. V. Varanasi, J. Liu, *Nano Lett.* **2012**, *12*, 4206.

[9] P. Simon, Y. Gogotsi, *Nat. Mater.* **2008**, *7*, 845.

[10] a) J. Liu, J. Jiang, C. Cheng, H. Li, J. Zhang, H. Gong, H. J. Fan, *Adv. Mater.* **2011**, *23*, 2076; b) R. Liu, S. B. Lee, *J. Am. Chem. Soc.* **2008**, *130*, 2942; c) L. F. Chen, Z. H. Huang, H. W. Liang, Q. F. Guan, S. H. Yu, *Adv. Mater.* **2013**, *25*, 4746.

[11] a) A. L. M. Reddy, M. M. Shaijumon, S. R. Gowda, P. M. Ajayan, *Nano Lett.* **2009**, *9*, 1002; b) S. Dong, X. Chen, L. Gu, X. Zhou, L. Li, Z. Liu, P. Han, H. Xu, J. Yao, H. Wang, *Energy Environ. Sci.* **2011**, *4*, 3502; c) J. Ren, L. Li, C. Chen, X. Chen, Z. Cai, L. Qiu, Y. Wang, X. Zhu, H. Peng, *Adv. Mater.* **2013**, *25*, 1155; d) C. Choi, J. A. Lee, A. Y. Choi, Y. T. Kim, X. Lepró, M. D. Lima, R. H. Baughman, S. J. Kim, *Adv. Mater.* DOI: 10.1002/adma.201304736.

[12] a) Z. Yu, B. Duong, D. Abbit, J. Thomas, *Adv. Mater.* **2013**, *25*, 3302; b) Y.-B. He, G.-R. Li, Z.-L. Wang, C.-Y. Su, Y.-X. Tong, *Energy Environ. Sci.* **2011**, *4*, 1288.

[13] J. Yan, E. Khoo, A. Sumboja, P. S. Lee, *ACS Nano* **2010**, *4*, 4247.

[14] X. Lu, T. Zhai, X. Zhang, Y. Shen, L. Yuan, B. Hu, L. Gong, J. Chen, Y. Gao, J. Zhou, Y. Tong, Z. L. Wang, *Adv. Mater.* **2012**, *24*, 938.

[15] X. Lu, G. Wang, T. Zhai, M. Yu, S. Xie, Y. Ling, C. Liang, Y. Tong, Y. Li, *Nano Lett.* **2012**, *12*, 5376.

[16] L. Yuan, X. H. Lu, X. Xiao, T. Zhai, J. Dai, F. Zhang, B. Hu, X. Wang, L. Gong, J. Chen, *ACS Nano* **2012**, *6*, 656.

[17] L. Bao, J. Zang, X. Li, *Nano Lett.* **2011**, *11*, 1215.

[18] P. Taberna, P. Simon, J.-F. Fauvarque, *J. Electrochem. Soc.* **2003**, *150*, A292.

[19] D. Pech, M. Brunet, H. Durou, P. Huang, V. Mochalin, Y. Gogotsi, P.-L. Taberna, P. Simon, *Nat. Nanotechnol.* **2010**, *5*, 651.

[20] J. A. Lee, M. K. Shin, S. H. Kim, H. U. Cho, G. M. Spinks, G. G. Wallace, M. D. Lima, X. Lepró, M. E. Kozlov, R. H. Baughman, *Nat. Commun.* **2013**, *4*, 1970.

[21] M. F. El-Kady, R. B. Kaner, *Nat. Commun.* **2013**, *4*, 1475.

[22] P. Yang, X. Xiao, Y. Li, Y. Ding, P. Qiang, X. Tan, W. Mai, Z. Lin, W. Wu, T. Li, H. Jin,P. Liu,J. Zhou,C. P. Wong, Z. L. Wang, *ACS Nano* **2013**, *7*, 2617.

[23] M. Kaempgen, C. K. Chan, J. Ma, Y. Cui, G. Gruner, *Nano Lett.* **2009**, *9*, 1872.

[24] M. F. El-Kady, V. Strong, S. Dubin, R. B. Kaner, *Science* **2012**, *335*, 1326.

[25] X. Lu, M. Yu, G. Wang, T. Zhai, S. Xie, Y. Ling, Y. Tong, Y. Li, *Adv. Mater.* **2013**, *25*, 267.

[26] J. Xu, Q. Wang, X. Wang, Q. Xiang, B. Liang, D. Chen, G. Shen, *ACS Nano* **2013**, *7*, 5453.

[27] X. Jiang, T. Herricks, Y. Xia, *Nano Lett.* **2002**, *2*, 1333.